An On-Chip Amplitude and Frequency Modulating Graphene-based Plasmonic Terahertz Signal Nano-Generator

Justin Crabb
crabb.j@northeastern.edu
Department of Electrical and Computer Engineering
Northeastern University
Boston, USA

Xavier Cantos-Roman
cantosroman.x@northeastern.edu
Department of Electrical and Computer Engineering
Northeastern University
Boston, USA

Gregory R Aizin
gregory.aizin@kbcc.cuny.edu
Department of Physics
Kingsborough College, The City University of New York
Brooklyn, USA

Josep M Jornet
j.jornet@northeastern.edu
Department of Electrical and Computer Engineering
Northeastern University
Boston, USA

ABSTRACT

An on-chip modulator-integrated graphene-based plasmonic nano-generator that operates in the terahertz band is presented. The device is based on a gated High Electron Mobility Transistor (HEMT). The use of graphene as the 2-Dimensional Electron Gas (2DEG) channel allows room temperature operation of large plasmonic oscillations which are highly tunable over a broad frequency range (1 to 2 THz). By implementing asymmetric boundary conditions at the source and drain, known as the Dyakonov-Shur (DS) instability, accelerated electrons excite plasmonic waves which reflect at the drain side of the channel. This induces Surface Plasmon Polariton (SPP) waves on the gate, which results in electromagnetic radiation in the THz region. By dynamically tuning these boundary conditions, the device operates with an integrated modulator. The device is numerically modeled and analyzed using an in-house developed multi-physics finite-difference platform based on the Hydrodynamic Model (HDM) for ballistic transport and Maxwell's equations for calculating the electromagnetic fields. After steady state is reached, the numerical analysis shows a clean waveform is possible with amplitude and frequency modulation capabilities. This device offers for the first time and in a compact form factor integrated generation, modulation and radiation functionalities.

CCS CONCEPTS

• **Hardware → Plasmonics**.

KEYWORDS

Plasmonics, Dyakonov-Shur, Graphene, TeraHertz, Modulator

NANOCOM '21, September 7–9, 2021, Virtual Event, Italy

ACM ISBN 978-1-4503-8710-1/21/09…$15.00
https://doi.org/10.1145/3477206.3477446

ACM Reference Format:
Justin Crabb, Xavier Cantos-Roman, Gregory R Aizin, and Josep M Jornet. 2021. An On-Chip Amplitude and Frequency Modulating Graphene-based Plasmonic Terahertz Signal Nano-Generator. In *The Eight Annual ACM International Conference on Nanoscale Computing and Communication (NANOCOM '21), September 7–9, 2021, Virtual Event, Italy.* ACM, New York, NY, USA, 6 pages. https://doi.org/10.1145/3477206.3477446

1 INTRODUCTION

The demand for faster internet has made a prominent impact on terahertz-band (0.1 to 10 THz) communication research over recent years, including the development of THz transceivers and antennas [1], propagation and channel models [2], and beyond-5G and towards-6G networking solutions [3], to name a few. Data rates of hundreds of Giga- and even Tera-bits-per-second (Tbps) will be required in the near future to provide sufficient internet to the increasing number of users. This is achievable only with larger bandwidths, which are easily available in the THz spectrum. While path loss phenomena such as molecular absorption and power spreading may divide the usable spectrum into smaller transmission windows at distances of tens of meters, these available windows offer bandwidths on the order of hundreds of GHz. At distances in the kilometer range, the performance is drastically impacted but several proposed approaches have been able to combat this issue [4, 5].

By tapping into the THz spectrum, many useful applications are achievable in the macro and nano scales, ranging from communication networks to imaging sensing applications. As data rates from fiber optic cables have increased drastically over the past few years, reaching the Pbps range [6], the demand for high speed wireless transmission continues to increase in which THz communication networks could help eliminate this bottleneck. At under 10 m, small cells and cell-free massive MIMO networks are proposed to drive the upcoming 6G networks reaching Tbps-level throughput [7]. In addition, long-distance sub-THz communication is achievable in [8, 9] reaching data rates of several Gbps.

Several nanoscale THz communication network applications have been proposed, including intrabody communication links for health monitoring, medical implant communication, and disease diagnosis/treatment [10]. Others include wireless network-on-chip for communication- and computation-intensive applications [11].

THz imaging and spectroscopy applications include non-metallic and metallic concealed weapon detection, explosive compound detection, pharmaceutical quality control, biology/medicine, and more [12].

Many THz sources have been developed in recent years [1], but in this paper we direct our focus to on-chip plasmonic resonant generators as they offer a compact structure needed for nanoscale applications. The most common field effect transistor (FET) devices are based on High Electron Mobility Transistors (HEMTs) which use III-V, III-N, and graphene for the 2-Dimensional Electron Gas (2DEG) channel. A similar device with room-temperature operation at 0.75 to 2.1 THz tunability is proposed in [13] using an Aluminum Gallium Nitride/Gallium Nitride-based HEMT. By using a Dual-Grating Gate (DGG) system we can potentially develop a device such as in [14] which is a InGaP/InGaAs/GaAs and/or InAl/InGaAs/InP based HEMT, offering room-temperature operation at 1 to 6 THz with up to 1 μW output power. The problem with these DGG devices are the high complexity in fabrication, relying on extremely precise methods.

2D structures that leverage graphene for the support of THz generation have also been proposed. For example, in [15] a graphene-gated HEMT with a III-V semiconductor channel is proposed. The plasma waves in the channel cavity are not directly radiated, but rather used to induce propagating Surface Plasmon Polariton (SPP) waves on the graphene surface. An external antenna is required, where the propagating SPP wave excites a graphene-based plasmonic nano-antenna, such as in [16]. By replacing the graphene gate with a metallic gate, such as in [17], we obtain a radiating plasmonic source.

In this paper, we develop the state-of-the-art multi-physics finite-difference simulation platform for numerical modeling a room-temperature operating on-chip THz plasmonic generator, and present the simulation results for numerical analysis. More specifically, the device is composed of a metallic-gated HEMT consisting of a graphene-layer 2DEG channel. By replacing the previously mentioned device's III-V channel with graphene, a higher 2D electron mobility is observed even at room temperature, offering larger well-defined plasmon resonances with a higher degree of tunability, allowing built-in modulation capabilities. The simplicity of source and modulation integration to the plasmonic device promotes its uniqueness from today's cutting edge THz generators. The device may be viewed of as a tunable generator, modulating source, or up-converter, as a waveform in the GHz range is input to the device and a modulated THz signal is produced. It can be shown from [18] that a graphene-based structure may be incorporated in our plasmonic generator to introduce phase modulation, allowing the development of a fully robust nano-transceiver ready for many THz applications such as macro and nano communication networks as well as spectroscopy and imaging.

The remainder of the paper is organized as follows. In Section 2, the proposed device is described along with the working principles and theory. Section 3 explains the numerical simulation platform for the device. The results from the platform are then discussed in section 4 for steady-state analysis as well as amplitude and frequency modulation. Finally, we conclude the paper in section 5.

2 DEVICE STRUCTURE AND THEORY OF OPERATION

Our proposed HEMT is composed of a $L = 1$ μm graphene channel, modeled as a 2DEG, sandwiched between two dielectric slabs of SiO_2 with a relative permittivity of 3.8. The top and bottom dielectric slabs have a corresponding depth of 20 nm and 400 nm. Two metallic contacts are placed along either side of the device which correspond to the source and drain contacts, with a third 1 μm metallic gate above the top dielectric slab which spans across the entire channel length, as shown in Figure 1. The HEMT device's resonant cavity is able to sustain plasmonic oscillations under the boundary conditions Dyakonov-Shur (DS) instability [19]. A current source is connected from the drain to source contacts, while a voltage source is connected from the gate to source contacts, in order to implement the DS asymmetric boundary conditions. The magnitudes of the constant DC supply from either source correlates either the device's operating frequency or its amplitude. Thus, an additional temporal variance to either source incorporates frequency or amplitude modulation into the plasmonic generator.

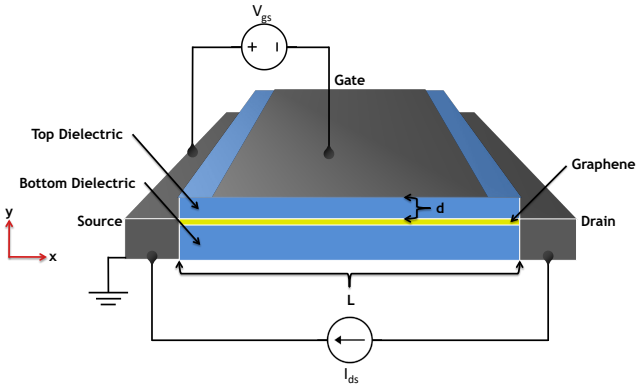

Figure 1: The proposed THz plasmonic device with a graphene channel.

The DS instability can be implemented in the device under asymmetric boundary conditions, specifically a zero-impedance AC-short circuit at the source and an infinite-impedance AC-open circuit at the drain. The voltage is held constant at the source, and the current is held constant at the drain. As the plasmons travel from source to drain under the current bias, these incident SPP waves experience a reflective gain due to the open circuit boundary condition. Alternatively, the reflected SPP waves undergo reflection at the short-circuit boundary without gain. After a small initial "kick" is given to the channel, represented by a small variation in current, the plasmonic oscillations travel back and forth inside the resonant cavity until steady state is reached, in which a quarter-wave plasmonic waveform continually oscillates in the cavity without experiencing any further gain. A higher drift velocity results in a higher reflective gain from the open-circuit boundary in the transient response, which ultimately leads to a shorter time for the SPP waves to reach steady state oscillations.

The device geometry and input parameters are limited by a few conditions in order for the instability to occur in the resonant cavity. First, the electrons which travel from the source to the drain at a velocity v must be able to reach the drain. This condition is met when $v > \frac{L}{\tau}$, where τ is the electron momentum relaxation time. This ensures the plasmonic oscillations reach the drain, where reflections occur, before the signal dies. The electron drift velocity is further bounded by the limit $v \ll v_F$, where $v_F = 1.5 \times 10^6\ \mathrm{m\,s^{-1}}$ is the Fermi velocity in the graphene 2DEG channel. At higher drift velocities, modeling equations break down as they become non-linear, and such high currents are not supported in the HEMT. Lastly, the condition $\omega\tau > 1$ allows the finite electron momentum relaxation time to appear infinite to the system, thus the fundamental frequency and all higher harmonics resonate in the cavity.

3 MULTI-PHYSICS PLATFORM MODELING EQUATIONS

A carefully chosen and vigorously fine-tuned model has been developed for the simulation platform of the plasmonic source. This state-of-the-art in-house finite difference platform is able to capture the physics of the proposed plasmonic device, offering reliable data for highly accurate numerical results. Specifically, the hydrodynamic model is able to capture ballistic transport phenomena within the device channel, while Maxwell's equations allow us to accurately calculate the electromagnetic field within and produced by the device. The sets of equations are discretized using Finite-Difference Time-Domain (FDTD) method, in which each cell has a set of parameters such as conductivity σ, permittivity ϵ, etc. Along the 2D channel, both Maxwell's and Hydrodynamic Model (HDM) equations are used for each cell, in which the resulting current from the HDM solver is used in Maxwell's equations, and the electric field values solved by Maxwell's are used in the HDM. It is worthy to note that since the device is uniform along the z-axis from Figure 1, only the 2D cross section of the HEMT is modeled.

3.1 Hydrodynamic Model

The HDM uses two main variables, namely, the electron density n and the electron current density j, each of which take on the average value associated to its cell. We relate the two parameters to the electron velocity via $j = nv$. As the boundary conditions for the DS instability require an AC-short circuit at the source and an AC-open circuit at the drain, we implement this in the simulation platform via $n_{x=0} = n_0$, and $j_{x=L} = j_0$, where n_0, j_0, and v_0 are the initial electron density, particle current density, and drift velocity values set across the device channel. This corresponds to the constant voltage held at the source and the constant current held at the drain, as shown in Figure 1. Before the simulation runs, we initialize a small "kick" in the current density at random locations along the channel in order for oscillations to begin, otherwise the device remains in a dormant state.

The two main HDM variables are updated using two equations, namely the continuity and Euler equations, obtained from the first two moments of the Boltzmann equation (a full derivation of the model is given in [20]). The continuity equation is given by

$$\frac{\partial n}{\partial t} = -\frac{\partial j}{\partial x}. \tag{1}$$

The next term we update is the particle current density j, given by the Euler equation

$$\frac{2 - B^2(x,t)}{2}\frac{\partial j(x,t)}{\partial t} + \frac{v_F\left(1 - B^2(x,t)\right)^{5/4}}{\sqrt{\pi}\hbar}\sqrt{n(x,t)}eE_x(x,t) + \frac{\left(j(x,t) - n(x,t)v_0\right)\left(1 - B^2(x,t)\right)^{5/4}}{\tau}\sqrt{\frac{n_0}{n(x,t)}} + \frac{v_F^2}{2}\left(1 - 2B^2(x,t)\right)\frac{\partial n(x,t)}{\partial x} + v_F B(x,t)\frac{\partial j(x,t)}{\partial x} = 0, \tag{2}$$

where $B(x,t) = \frac{v(x,t)}{v_F}$ is the dimensionless local drift velocity. The second term is the field equation which has the input E_x from Maxwell's equations, followed by the collision term which introduces the effects of scattering from phonons and impurities within the 2DEG channel. Following, we have the pressure term which uses a previously calculated $\frac{\partial n(x,t)}{\partial x}$, and lastly we have the convective term. In order to improve accuracy, it is best to update the first four terms of the Euler equation, then compute $\frac{\partial j(x,t)}{\partial x}$ using a weighted upwind scheme, followed by the last convective term in the Euler equation.

We briefly introduce the plasma velocity v_p, representing the velocity of plasma waves within the graphene electron fluid [21],

$$v_p = \sqrt{\frac{v_F^2}{2} + \frac{e^2\sqrt{n_0}dv_F}{\sqrt{\pi}\epsilon\hbar}}. \tag{3}$$

As the plasmonic oscillations are the dominant mechanism for the THz signal generation, we can directly relate v_p to the device's resonant fundamental frequency via a simplified formula

$$f_0 = \frac{v_p}{4L}, \tag{4}$$

for quarter-wave plasmonic cavity resonance due to asymmetric boundary conditions. For symmetric boundary conditions the plasmonic cavity supports oscillations at half-wavelengths, resonating at a frequency twice as large.

By introducing a temporal variance to n_0 or j_0, the resulting waveform at steady state may be fully modulated. This can be done by setting the parameters equal to a sinusoidal waveform centered at the initial value of n_0 or j_0. As in (4), the resonant frequency of the cavity depends on v_p, which depends on electron density n_0. Thus, by modulating the electron density at the source we can modulate the resonant frequency of the plasmonic oscillations within the cavity. On the other hand, by tuning the current density j_0 at the drain contact we can modulate the amplitude of the plasmonic oscillations. We numerically investigate the performance of these modulation capabilities in Section 4.3.

3.2 Maxwell's Equations

The previously analyzed hydrodynamic model describes electron transport within the 2DEG channel, producing the electron current density j. This term is used to calculate the current density $J_x =$

$-e(j - j_0)$, an input to Maxwell's equations given by

$$\nabla \times \boldsymbol{E} = -\mu_0 \frac{\partial \boldsymbol{H}}{\partial t},$$
$$\nabla \times \boldsymbol{H} = \boldsymbol{J} + \epsilon\epsilon_0 \frac{\partial \boldsymbol{E}}{\partial t}, \tag{5}$$

where $\boldsymbol{E} = E_x\hat{\boldsymbol{x}} + E_y\hat{\boldsymbol{y}}$ and $\boldsymbol{H} = H_z\hat{\boldsymbol{z}}$ are the electric and magnetic components of the EM field induced by fluctuations of the electric current in the 2DEG channel $\boldsymbol{J} = J_x\hat{\boldsymbol{x}}$. The electrodynamic equations are discretized using FDTD based on [22], which introduces the Yee algorithm for computational electrodynamics. The grid space is divided into cells in which E_x, E_y, and H_z are defined at different locations of the cells. Using neighboring values for each term, the electromagnetic field is calculated in each cell, and the E_x term is input to the field term of the Euler equation. The FDTD discretization method is described in more detail in [17].

4 NUMERICAL RESULTS

The aforementioned HDM and EM equations are combined and discretized using FDTD to develop a multi-physics simulation platform for the proposed device. The platform offers reliable and accurate results for designing, tuning, and analyzing the device. Commercial tools do not allow simultaneous calculation of both models in the time-domain, thus the FDTD simulation platform was adapted to allow the solvers to run simultaneously on Matlab.

4.1 The Platform

The simulation platform allows us to model and explore the performance of the proposed device to generate sustained plasmonic oscillations in the 1 to 2 THz range, and modulate the generated signal either in amplitude or in frequency. The spatial increment within the 2DEG is limited by the Debye criteria, $dx < \sqrt{\frac{\epsilon\kappa T}{n}}$, to $dx = 5$ nm [23]. This condition is applied to both HDM and EM models, with a time increment of $dt = \frac{dx}{2c}$, where c is the speed of light. The HDM solver is applied along the 2DEG graphene channel, spanning across the x-axis and located at the boundary between two adjacent dielectric cells. Thus, the 2DEG is modeled in an infinitely thin sheet of zero thickness.

The asymmetric boundary conditions previously mentioned are required for the generation of sustained plasmonic oscillations in the channel of the HEMT device. The initial parameters in the HDM were set to $n_0 = 4.2 \times 10^{16}$ m^{-2}, $v_0 = 4 \times 10^5$ m s^{-1}, $L = 1$ µm, and $\tau = 5$ ps. Upon such conditions, the platform is able to generate a signal set at 1.2 THz. Although lower electron relaxation times are acceptable, an increased value beyond the theoretical lower limit is used to allow cleaner waveforms for demonstration purposes.

4.2 THz Plasmonic Source

The procedure analyzed in section 3 constitutes the numerical platform for modeling the THz plasmonic source. Throughout the course of the simulation, the EM field terms E and H are continually measured within the channel. The x-component of the electric field induced from temporal evolution of current oscillations within the device channel and the spectrum calculated from the measured electromagnetic field are shown in Figure 2. The time-domain signal is shown on the left, where we see the initial transient response eventually reach steady state at about 40 ps. This transient time may be reduced by increasing either the electron relaxation time τ or the initial drift velocity v_0. On the right side of the figure, we see the frequency-domain spectrum showing the fundamental frequency at 1.2 THz, as well as all higher harmonics that satisfy $\omega\tau > 1$ at 1.2 THz increments.

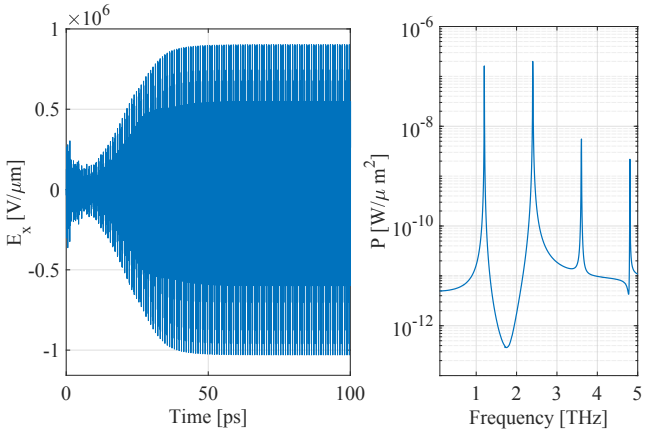

Figure 2: Time domain of the x-component of the electric field E_x on the left with 1.2 THz resonance in the HEMT channel cavity shown on the right.

The conditions for growth of plasmonic oscillations within the 2DEG under asymmetric boundary conditions examined in section 2 are thoroughly tested for the platform. The condition $v_0 > \frac{L}{\tau}$ is not satisfied for low v_0, large L, or low τ, in which the resonant cavity suppresses the current oscillations due to lack of gain reflections and an attenuated signal is observed. A decay in plasmonic oscillations is also observed when the DS boundary conditions are not held or reversed. Numerical analysis shows unstable results with drift velocities above $0.6v_F$, in which (2) becomes non-linear and the AC current in the 2DEG blows up to infinity. The dependence of fundamental frequency resonating in the cavity on L, d, or n_0 matches the theory provided from (4).

4.3 Modulation

Upon conversion of the DC boundary sources to AC, modeled by a temporal variance in the electron density centered at n_0 or in current density centered at j_0, modulation of current oscillations in the channel is obtained. By modulating $n_{x=0}$ we can vary the frequency of the signal, and by modulating $j_{x=L}$ we can vary the amplitude. This can be modeled by setting either to a sinusoidal waveform with a frequency f_M and an amplitude of A_M with a DC offset, $X_0(1 + A_M \sin(2\pi f_M t))$, where X_0 is either n_0 or j_0. It is worthy to note that any variation in either source varies the total input DC power to the device, thus when tuning the source electron density we also observe slight amplitude modulation.

4.3.1 Amplitude Modulation. The response of the produced electric field component to various DC drain currents can be used for static analysis on amplitude dependence for AM capabilities. The modulator is turned off, that is the modulation parameters

$A_M = f_M = 0$, and the steady-state signal remains fixed in amplitude and frequency for various drain currents. Figure 3 shows the amplitude of the x-component of the electric field E_x measured during steady-state in response to a range of drain currents J applied to the device, given by $-ej_0$.

The responsivity can be defined as the first derivative of the linear fitted curve, determining how the device responds to a change in applied current density. This can be calculated as $\frac{\Delta E_x}{\Delta J}$, and thus simple analysis from Figure 3 shows an obtainable responsivity of 690 VA^{-1}.

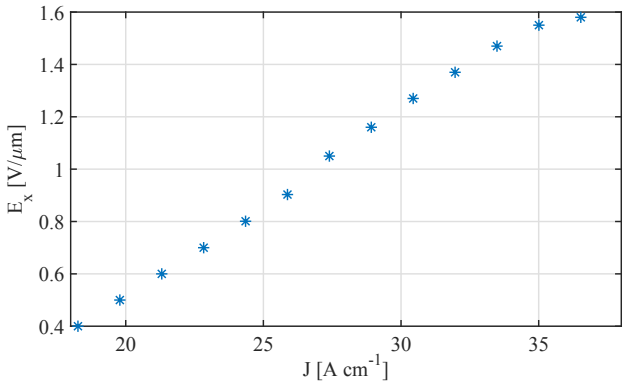

Figure 3: Measured electric field x-component E_x as a function of applied drain current J.

The static analysis on amplitude dependence provides insight for selecting the initial and modulation parameters of our AM device. Figure 4 shows the device running with $F_M = 80$ GHz and $A_M = 30\%$ of the initial parameter value, centered at 23 A cm^{-1}. As shown in the figure, the modulation starts after 60 ps in order for the original signal to reach steady-state before switching the DC drain current to AC. The effects of the modulated boundary condition on the resulting resonating signal are shown, in which there is a small "shifting time" between the modulating $j_{x=L}$ signal (orange) and the modulated signal (blue). The plasmons must travel back and forth within the channel cavity a few times in order to react to the change in the modulation parameter. Thus, a high f_M or A_M causes the transient response to take over the signal's modulation effects, which can be avoided by increasing v_0 or τ.

We introduce a theoretical limit of the modulation frequency f_M as $\frac{1}{\tau} = \frac{1}{5\,\text{ps}} = 200$ GHz. However, we have concluded that the device's reaction to amplitude-tunable parameters have a larger transient time than frequency-tunable parameters, and thus the responsivity for the AM signal decreases as we approach this theoretical limit. Specifically, modulating j_0 at higher frequencies does not allow the amplitude of the blue signal to respond fast enough to the varying orange signal, as the "shifting times" are comparable to the modulation period and the resulting changes in amplitude of the blue signal begins to reduce. Thus, the AM is still present at such high frequencies (up to 170 GHz), but the resulting variation in amplitude of the blue signal is reduced. In ranges of $f_M = 50$ to 100 GHz we see a resulting responsivity of 400 to 200 VA^{-1}, respectively, when the amplitude of the modulation is $A_M = 30\%$.

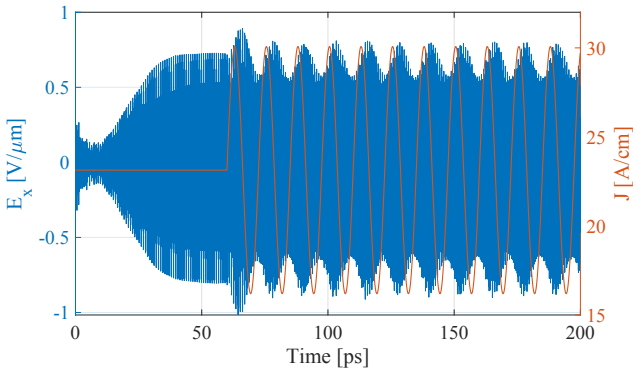

Figure 4: Modulated electric field x-component E_x (blue) as a function of time in response to a varying applied current density J (orange). The applied signal has a modulating frequency of 100 GHz and an amplitude of 30%.

4.3.2 Frequency Modulation. Similar to the AM analysis, we first run the device with zero modulation to show the response. The HEMT resonant frequency dependence can be demonstrated from Figure 5 under corresponding changes in n_0 at the source. We have the theoretical curve (shown in blue) arising from (4) for quarter-wave plasmonic oscillations. The experimental points represent zero-modulation with various n_0 values, which the device's operating resonant frequency shows dependence on (note that the small deviation in the analytical and numerical results are caused by the idealized character of the theoretical formula, in which the gate-to-channel distance d is assumed to be zero). The FM responsivity may be defined as the change in resonant frequency in response to the change in the electron density n_0. Thus, our responsivity given by $\frac{\Delta f_0}{\Delta n_0}$ ranges from 18.55×10^{-6} to 4×10^{-6} Hz m^{-2} for $n_0 = 1 \times 10^{16}$ to 5×10^{16} m^{-2}.

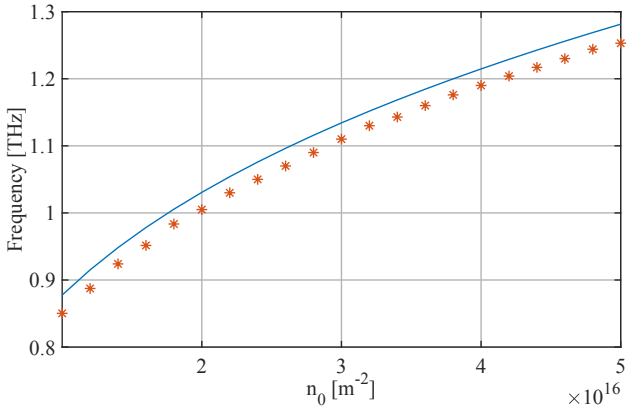

Figure 5: Resonant frequency dependence on applied electron density n_0. The theoretical curve is shown with the blue line, while experimental points are shown in orange.

The spectrum of the FM modulated device is shown in Figure 6, where modulation parameters $A_M = 30\%$ and $f_M = 180$ GHz are

chosen. For demonstration purposes, we show the second harmonic response in Figure 6 as the first harmonic FM is not as clear. We see the device is capable of about 360 GHz modulation bandwidth, centered at 2.21 THz. Here, the field components are measured within the device channel, giving us the output power in $\mathrm{W\mu m^{-2}}$. The FM signal was ran at modulation frequencies f_M near the theoretical limit of 200 GHz, and has shown successful FM signals at 200 GHz and unsuccessful results at higher frequencies.

The responsivity of the device from the numerical standpoint can simply be calculated in the same approach as previously mentioned. For analyzing the equivalent first harmonic provided from Figure 6, we have a modulation bandwidth of 360 GHz/2 = 180 GHz. Thus, with a 30% amplitude modulation A_M, with n_0 centered at 3.1×10^{16} $\mathrm{m^{-2}}$, we attain a responsivity of 9.67×10^{-6} $\mathrm{Hz\,m^{-2}}$.

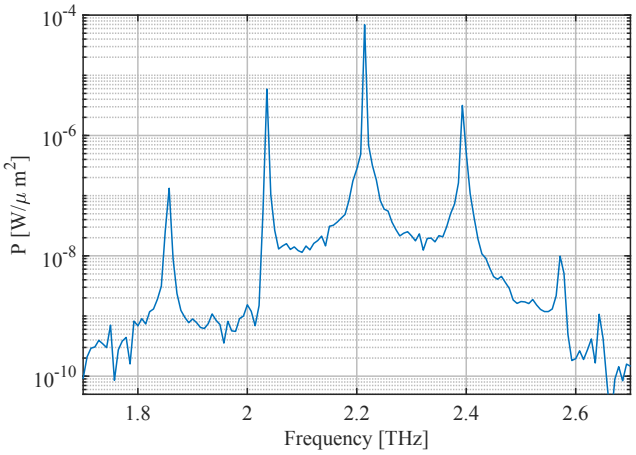

Figure 6: Frequency spectrum of the device's resulting FM signal in response to a varying n_0. The applied signal has a frequency of 180 GHz **and an amplitude of 30%.**

5 CONCLUSION

In this paper, we have demonstrated the first frequency and amplitude tunable on-chip plasmonic THz generator, in which the configuration is based on a HEMT device. Asymmetric boundary conditions with source voltage and drain current allow plasmonic oscillations to occur in the graphene 2DEG channel, causing the channel to behave as a resonant cavity for quarter-wave plasmonic oscillations. Utilizing an in-house-developed FDTD platform, we have demonstrated the device signal generation and modulation capabilities. In particular, we have shown that both amplitude and frequency modulation are possible, with modulation bandwidths approaching 200 GHz, opening the door to ultrabrodband communication systems. The engineering of tailored waveforms and modulation schemes that maximize the achievable data-rate and minimize the bit error rate are part of our future work

6 ACKNOWLEDGEMENTS

This work was partially supported by the Air Force Office of Scientific Research (AFOSR) under Grant no. FA9550-16-1-0188, and the US National Science Foundation under Grant no. CNS-2011411.

REFERENCES

[1] Kaushik Sengupta, Tadao Nagatsuma, and Daniel M Mittleman. Terahertz integrated electronic and hybrid electronic–photonic systems. *Nature Electronics*, 1(12):622–635, 2018.
[2] Chong Han and Yi Chen. Propagation modeling for wireless communications in the terahertz band. *IEEE Communications Magazine*, 56(6):96–101, 2018.
[3] Michele Polese, Josep Miquel Jornet, Tommaso Melodia, and Michele Zorzi. Toward end-to-end, full-stack 6g terahertz networks. *IEEE Communications Magazine*, 58(11):48–54, 2020.
[4] Swen Koenig, Daniel Lopez-Diaz, Jochen Antes, Florian Boes, Ralf Henneberger, Arnulf Leuther, Axel Tessmann, René Schmogrow, David Hillerkuss, Robert Palmer, et al. Wireless sub-thz communication system with high data rate. *Nature photonics*, 7(12):977–981, 2013.
[5] Qiuyu Wu, Changxing Lin, Bin Lu, Li Miao, Xin Hao, Zhaohui Wang, Yi Jiang, Wenqiang Lei, Xianjing Den, Hongbin Chen, et al. A 21 km 5 gbps real time wireless communication system at 0.14 thz. In *2017 42nd International Conference on Infrared, Millimeter, and Terahertz Waves (IRMMW-THz)*, pages 1–2. IEEE, 2017.
[6] Peter J Winzer, David T Neilson, and Andrew R Chraplyvy. Fiber-optic transmission and networking: the previous 20 and the next 20 years. *Optics express*, 26(18):24190–24239, 2018.
[7] Ian F Akyildiz, Ahan Kak, and Shuai Nie. 6g and beyond: The future of wireless communications systems. *IEEE Access*, 8:133995–134030, 2020.
[8] Ingmar Kallfass, Florian Boes, Tobias Messinger, Jochen Antes, Anns Inam, Ulrich Lewark, Axel Tessmann, and Ralf Henneberger. 64 gbit/s transmission over 850 m fixed wireless link at 240 ghz carrier frequency. *Journal of Infrared, millimeter, and terahertz waves*, 36(2):221–233, 2015.
[9] Akihiko Hirata, Toshihiko Kosugi, Hiroyuki Takahashi, Ryouichi Yamaguchi, Fumito Nakajima, Tomofumi Furuta, Hiroshi Ito, Hirohiko Sugahara, Yasuhiro Sato, and Tadao Nagatsuma. 120-ghz-band millimeter-wave photonic wireless link for 10-gb/s data transmission. *IEEE transactions on microwave theory and techniques*, 54(5):1937–1944, 2006.
[10] Hadeel Elayan, Raed M Shubair, Josep Miquel Jornet, and Pedram Johari. Terahertz channel model and link budget analysis for intrabody nanoscale communication. *IEEE transactions on nanobioscience*, 16(6):491–503, 2017.
[11] Quoc-Tuan Vien, Michael Opoku Agyeman, Tuan Anh Le, and Terrence Mak. On the nanocommunications at thz band in graphene-enabled wireless network-on-chip. *Mathematical Problems in Engineering*, 2017, 2017.
[12] John Federici and Lothar Moeller. Review of terahertz and subterahertz wireless communications. *Journal of Applied Physics*, 107(11):6, 2010.
[13] A El Fatimy, N Dyakonova, Y Meziani, T Otsuji, W Knap, S Vandenbrouk, K Madjour, D Theron, C Gaquiere, MA Poisson, et al. Algan/gan high electron mobility transistors as a voltage-tunable room temperature terahertz sources. *Journal of Applied Physics*, 107(2):024504, 2010.
[14] Taiichi Otsuji, Takayuki Watanabe, Stephane Albon Boubanga Tombet, Akira Satou, Victor Ryzhii, Vyacheslav V Popov, and Wojciech Knap. Emission and detection of terahertz radiation using two-dimensional plasmons in semiconductor nanoheterostructures for nondestructive evaluations. *Optical Engineering*, 53(3):031206, 2013.
[15] Josep Miquel Jornet and Ian F Akyildiz. Graphene-based plasmonic nano-transceiver for terahertz band communication. In *The 8th European conference on antennas and propagation (EuCAP 2014)*, pages 492–496. IEEE, 2014.
[16] Josep Miquel Jornet and Ian F Akyildiz. Graphene-based plasmonic nano-antenna for terahertz band communication in nanonetworks. *IEEE Journal on selected areas in communications*, 31(12):685–694, 2013.
[17] Mona Nafari, Gregory R Aizin, and Josep M Jornet. Plasmonic hemt terahertz transmitter based on the dyakonov-shur instability: Performance analysis and impact of nonideal boundaries. *Physical Review Applied*, 10(6):064025, 2018.
[18] Prateek K Singh, Gregory Aizin, Ngwe Thawdar, Michael Medley, and Josep Miquel Jornet. Graphene-based plasmonic phase modulator for terahertz-band communication. In *2016 10th European Conference on Antennas and Propagation (EuCAP)*, pages 1–5. IEEE, 2016.
[19] Michael Dyakonov and Michael Shur. Shallow water analogy for a ballistic field effect transistor: New mechanism of plasma wave generation by dc current. *Physical review letters*, 71(15):2465, 1993.
[20] J Crabb, X Cantos, G Aizin, and J Jornet. Hydrodynamic theory of dyakonov-shur instability in graphene transistors. *Physical Review B*, 2021.
[21] D Svintsov, V Vyurkov, V Ryzhii, and T Otsuji. Hydrodynamic electron transport and nonlinear waves in graphene. *Physical Review B*, 88(24):245444, 2013.
[22] Allen Taflove and Susan C Hagness. *Computational electrodynamics: the finite-difference time-domain method*. Artech house, 2005.
[23] Mohammad Ali Khorrami, Samir El-Ghazaly, Hameed Naseem, and Shui-Qing Yu. Global modeling of active terahertz plasmonic devices. *IEEE Transactions on Terahertz Science and Technology*, 4(1):101–109, 2013.